Theoretical Chemistry Accounts (2023) 142:118
https://doi.org/10.1007/s00214-023-03060-2

RESEARCH

On the decomposition mechanism of propanal: rate constants evaluation and kinetic simulations

Andrea Della Libera[1] · Maristella Di Teodoro[1] · Matteo Pelucchi[1] · Carlo Cavallotti[1]

Received: 28 July 2023 / Accepted: 2 October 2023 / Published online: 26 October 2023

Abstract
The reactivity of aldehydes has been the subject of considerable interest in chemical kinetics, with propanal often chosen as the representative species. Despite its relevance, the reactivity of propanal is currently estimated from analogy and fitting of experimental data measured in limited temperature and pressure ranges, while the few literature theoretical studies have focused more on the exploration the potential energy surface (PES) than on the estimation of rate constants. The purpose of this work is to reinvestigate the propanal decomposition kinetics using the ab initio transition state theory based master equation approach with the intent of: (1) Determining accurate rate constants of key reaction channels; (2) Updating and validating an existing kinetic model by simulating available experimental data on propanal pyrolysis. It is found that propanal decomposition at the initial stages of pyrolysis occurs through four unimolecular barrierless reactions to form $CHO + C_2H_5$, $CH_2CHO + CH_3$, $CH_3CHCHO + H$, and $CH_3CH_2CO + H$, and a termolecular pathway leading to the formation of $C_2H_4 + CO + H_2$. High pressure rate constants were determined for each barrierless reaction channel using Variable Reaction Coordinate Transition State Theory and used to estimate phenomenological temperature and pressure dependent channel specific rate constants integrating the 1 dimensional master equation over the whole PES. The decomposition rate constants so determined are in agreement with the few available experimental data and significantly faster than previous literature estimates. The estimated kinetic parameters were finally implemented into the CRECK kinetic mechanism, leading to an improved agreement with shock tube pyrolysis data from the literature.

Keywords Propanal · Aldehydes · Transition state theory · Kinetic simulations · Master equation · VRC-TST · Pyrolysis

1 Introduction

Aldehydes are formed as intermediate species or products in many gas phase reactive systems of interest to the chemical kinetics community. They are recognized as possible precursors of complex organic molecules in the interstellar medium [1, 2] and are preferentially formed in low temperature combustion environments from any hydrocarbon fuel [3]. Moreover, the interest in pyrolysis and combustion of carbonyl compounds has increased due to the recent surge in popularity of sustainable fuels from biomass [4]. These are indeed complex mixtures of hydrocarbons carrying the chemical functionalities of the starting feedstock with high concentrations of oxygenated species with one or more substitutions (e.g. $–OCH_3$, –OH). On one hand, such fuels are found to inhibit soot formation, on the other hand they lead to the formation of toxic side products, such as aldehydes and acids. High concentrations of oxygenated pollutants have been observed in exhaust gases from internal combustion engines [5, 6] and from gasification processes of biomass wastes [7]. An experimental investigation by Pang et al. [8] examined the carbonyl emissions from a biodiesel–ethanol–diesel blend and a conventional diesel fuel from fossil sources in internal combustion engine experiments. At every speed and engine load conditions investigated the most abundant carbonyl compounds, from the highest to the lowest, were acetaldehyde, formaldehyde, acetone, and propanal, thus highlighting the importance of investigating the reactivity of C_3 oxygenated molecules. Also, low molecular weight molecules carrying different oxygenated functional groups (e.g. carbonyl, hydroxyl) are useful representative compounds to describe the reactivity of higher molecular weight molecules belonging to the same

✉ Carlo Cavallotti
carlo.cavallotti@polimi.it

[1] Dipartimento di Chimica, Materiali e Ingegneria Chimica, Politecnico di Milano, 20131 Milan, Italy

family by means of the definition of analogy based rate rules [9].

Among the C_3 oxygenated compounds, n-propanol and iso-propanol are probably the most largely characterized due to the long lasting interest in alcohol fuels. The combustion of propanol isomers has been widely analysed through experimental studies and modelling validations [10] in several reactor configurations [11], also pointing at the key role of aldehydes carrying the same C_3 backbone in fuel ignition and flame propagation experiments [12]. The number of literature studies on propanal (C_2H_5CHO) however, is significantly more limited, although it is generally included in core subsets of kinetic mechanisms and used as an archetypal species to describe the pyrolysis and oxidation of other organic compounds, including C_{3+} aldehydes [13, 14]. Overall, the characterization of propanal reactivity in pyrolysis and oxidation environments is of relevance to many aspects of sustainable energy, waste valorization, and climate change mitigation and emissions reduction [15]. A good number of detailed kinetic models have been proposed in the literature [16–25]. However, the kinetics of primary unimolecular decomposition steps has not been addressed with state of the art fundamental approaches.

The decomposition mechanism of propanal was first investigated by Lifshitz et al. [18]. The thermal decomposition of propanal in argon was studied in a single-pulse shock tube behind reflected shocks over the 970–1300 K temperature range. They identified and quantified the main decomposition products with their relative abundance and proposed a free radical chain mechanism initiated by two unimolecular decomposition reactions:

$$C_2H_5CHO \rightarrow C_2H_5 + CHO \quad \text{(R1)}$$

$$C_2H_5CHO \rightarrow CH_3 + CH_2CHO \quad \text{(R2)}$$

Propanal decomposition was successfully modelled with a reaction scheme containing 22 species and 52 elementary reactions. Later, Kasper et al. [17] measured the concentration of several species, including radicals, in a stoichiometric propanal premixed flat flame using molecular beam mass spectroscopy. At a pressure of 5000 Pa and temperatures in the 1000–1500 K range, they observed the formation of C_4–C_6 oxygenated molecules, which were hypothesized to derive from C_1–C_3 radical additions to C_2H_5CHO or C_3H_4O. Only a qualitative proposal for the overall mechanism was made, highlighting the need for a comprehensive detailed kinetic model. Veloo et al. [16] pointed out the poor number and the limitations of previous experimental and modelling studies proposing new laminar flame speed measurements, jet stirred reactor speciation data, and a detailed kinetic model including 1618 reactions and 327 compounds to interpret the experimental findings. In 2015, Pelucchi et al. [19] presented new single-pulse shock tube data and ignition delay times for the series of C_3–C_5 linear aldehydes (i.e., propanal, n-butanal, and n-pentanal) and released pyrolysis and high temperature oxidation sub-mechanisms, coupled to two known kinetic frameworks: the NUIG mechanism [26–30] and the CRECK model [19, 31–33]. Reaction classes included unimolecular initiation and H-abstraction reactions, radical decompositions, and isomerizations. The initiation reactions included the unimolecular dissociations to ethyl (R1) and methyl (R2) hypothesized by Lifshitz [18], in addition to three different H loss channels:

$$C_2H_5CHO \rightarrow CH_3CH_2CO + H \quad \text{(R3)}$$

$$C_2H_5CHO \rightarrow CH_3CHCHO + H \quad \text{(R4)}$$

$$C_2H_5CHO \rightarrow CH_2CH_2CHO + H \quad \text{(R5)}$$

Temperature and pressure dependent rate constants were estimated from the inverse radical–radical recombination process by applying a simplified three frequency version of QRRK/MSC [34] that is, nowadays, largely overcome. The predicted branching ratios for R1-R5 were 66.5, 32.9, 0.6, 0.0, 0.0 at 1000 K and 65.6, 31.4, 2.7, 0.2, 0.1 at 1500 K, respectively. Both NUIG and CRECK mechanisms reproduced the experimental behaviour of propanal in terms of temperature dependence of fuel decomposition and of products profiles, with some deviation in acetylene predictions and underestimating the concentrations of propane and propene.

Only a few theoretical studies have investigated propanal reactivity. Chin and Lee [35] investigated the singlet C_3H_6O PES, accessed from C_2H_5CHO, including both bi- and termolecular decomposition channels. Geometries and frequencies were obtained with Density Functional Theory (DFT) at the B3LYP/6-311G(d,p) level, while energies were estimated at the CCSD(T)/6-311G(3df,2p) level. It was found that, in addition to the R1-R5 barrierless decomposition processes, a sixth termolecular decomposition channel contributes to propanal reactivity:

$$CH_3CH_2CHO \rightarrow C_2H_4 + CO + H_2 \quad \text{(R6)}$$

The calculated energy barrier and reaction enthalpy are 72.2 and 26.7 kcal/mol, while reaction energies for the formation of ethyl (R1) and methyl (R2) radicals were 80.6 and 81.1 kcal/mol, respectively. Branching ratios were computed using RRKM theory for the molecular channels and Variational Transition State Theory (VTST) for barrierless bond fissions. The reported secondary channels included direct dissociation to CO and ethane (barrier of 83.7 kcal/mol), loss of H_2 (barrier of 77.1 kcal/

mol), propanal isomerization from cis (minimum energy) to gauche configuration, and homolytic H loss from the carbonyl group. Cavallotti et al., who studied extensively the reaction of $O(^3P)$ with unsaturated hydrocarbons using the ab initio transition state theory-based master equation (AITSTME) approach [36–40], recently investigated the portion of the C_3H_6O triplet PES accessed from the addition of $O(^3P)$ to propene [41, 42]. It was found that it can lead, upon terminal addition of oxygen to propene and Intersystem Crossing (ISC), to the singlet PES and eventually to the formation of propanal. Stationary points and transition states were studied at the CASPT2/aug-cc-pVTZ level with active spaces of different size. The energies of wells that did not exhibit multireference behavior were also computed at the CCSD(T) level with extrapolation to the complete basis set (CBS). The reactivity over the C_3H_6O PES was studied determining RRKM microcanonical rate constants and integrating stochastically the 1D master equation (ME), explicitly accounting for hindered rotations and including tunnelling contributions. The singlet state propanal PES included dissociations to ethyl and methyl (R1, R2), the termolecular decomposition channel (R6), and isomerization to methyl oxirane, which has a barrier higher than R6. Rate constants of barrierless reactions were determined with VTST.

In the present work the propanal singlet PES is re-examined with the intent of determining the main decomposition pathways in large temperature and pressure ranges. On the basis of the previous experimental and theoretical findings discussed above it was decided to focus the investigation on the R1-R4 barrierless decomposition reactions, and on R6 decomposition to ethylene, carbon monoxide, and molecular hydrogen, which is expected to be the fastest among the activated molecular channels. It should be noted that the level of theory used in the present work is much higher both with respect to the simple estimate based on analogy for high pressure rate constants, as well as for the QRRK estimate of the pressure dependence used in previous studies [19]. As a consequence, we expect that the rate constants determined in this work with state of the art computational methodologies constitute a significant step forward in the understanding of the chemical reactivity of aldehydes.

To explore the impact on existing mechanisms, the computed rate constants were implemented in the latest version of the CRECK kinetic mechanism and used to simulate experimental data from the literature. The paper is organized as follows: the theoretical approach and methodology are described in Sect. 2. Section 3 reports the results covering the PES investigation, the determination of decomposition and recombination reaction rate constants, and the impact of these on kinetic simulations of the pyrolysis experiments of Lifshitz et al. [18] and Pelucchi et al. [19].

2 Methods

2.1 Ab initio simulations and rate constants estimation

The reactivity of propanal was theoretically investigated using the AITSTME approach [43] to compute rate constants for the main reaction channels: homolytic bond scissions to produce ethyl, methyl, or hydrogen radicals (R1–R4), their reverse recombination ($R1_B$–$R4_B$), and the 3-body dissociation (R6). Structures, gradients, and Hessians of all stationary points, saddle points, and van der Waals wells were determined at the ωB97X-D/aug-cc-pVTZ level using an ultrafine grid [44]. A conformational analysis over selected dihedral angles was performed at the ωB97X-D level with the 6–311 + G(d,p) basis set with the aim of determining minimum energy structures. An Intrinsic Reaction Coordinate (IRC) scan was performed for the R6 reaction at the ωB97X-D/jun-cc-pVTZ level. Internal torsional motions characterized by low energy barriers were treated as hindered rotors with hindrance potentials determined at the ωB97X-D/6–311 + G(d,p) level. Energies were computed at the CCSD(T)/aug-cc-pVTZ level and corrected for the inclusion of core electrons correlation at the CCSD(T,core)/cc-pCVTZ level. An extrapolation to the complete basis set (CBS) limit was performed using the scheme proposed by Martin [45] and density fitted (DF) MP2 energies, as recently described in [46]. On the basis of extensive comparison with experimental data, we expect that the accuracy of this method is within 1 kcal/mol, or better, for 0 K reaction energy changes and of similar accuracy for energy barriers for systems that do not present multireference character. When available, energy differences were compared with the Active Thermochemical Tables (ATcT) [47, 48] values and literature theoretical estimates.

The rate constant for reaction R6, the only one with a barrier among those investigated, was determined using microcanonical variational transition state theory, as implemented in MESS [49], using vibrational frequencies computed after converting the Hessian in internal coordinates, using the algorithms implemented in EStokTP [50]. Rate constants of barrierless reactions were determined using variable reaction coordinate transition state theory (VRC-TST) [51–53], as implemented in VaReCoF [54], using the semi-automatized procedure implemented in EStokTP. Briefly, the adopted approach consists in determining the minimum energy path (MEP) by performing constrained optimizations as a function of the breaking bond coordinate for about 10 points in the 2–4 Å range. Structures, energies, and Hessian for each point along the MEP were determined at the CASPT2/jun-cc-pVTZ level

using a (4e,4o) active space consisting of the σ and σ* bonding and antibonding orbitals of the breaking bond and of the π and π* orbitals of the carbonyl group. All CASPT2 calculations were performed using an IPEA level shift of 0.25. In order to test the impact of the size of the active space on the simulation results, for R2 a larger (10e,9o) active space was used. In addition to the (4e,4o) active space described above, it included the oxygen lone pair (2e,1o), and the C–O and C–C σ and σ* orbitals of the CH_2CHO fragment (4e,4o). High level single point energies were determined for each optimized structure at the CASPT2(4e,4o)/aug-cc-pVTZ level. The correction potential used for VRC-TST simulations consists of two terms: geometry relaxation and high level energy correction. It was computed through two separate calculations: a constrained optimization performed at the CASPT2(4e,4o)/jun-cc-pVTZ level, in which the fragment geometries are kept rigid and the only degrees of freedom that are optimized are the five that determine the relative position of the fragments, and a CASPT2(2e,2o)/cc-pVDZ calculation performed using the same geometry adopted to compute the high level energy. The differences between complete and constrained geometry optimization and between high level single point and CASPT2(2e,2o)/cc-pVDZ energies determine the two additive terms of the correction potential. The correction potential was then added to the energies determined in the stochastic scan performed over the dividing surfaces by VaReCoF, which is used to determine the information necessary to estimate the reactive fluxes. Single point energies in VRC-TST simulations were determined at the CASPT2(2e,2o)/cc-pVDZ level, using an active space composed of the σ and σ* orbitals of the breaking bond.

VRC-TST calculations were performed using multifaceted spherical dividing surfaces constructed from pivot points placed along the breaking bond, whose direction vector was determined from a constrained optimization performed at a fragment separation of 2.4 Å. This geometry was chosen as reference as it allows identifying properly the direction of maximum interaction between the orbitals of the radical centers of the two fragments, thus that of the breaking bond, not only for this geometrical configuration, but for all the minimum energy geometries encountered along the reaction path during the recombination process, as found during the MEP scan that is performed preliminarily to VRC-TST calculations. It should be noted that pivot points are shifted in VRC-TST to minimize variationally the reaction flux. Two pivot points, displaced perpendicularly to the molecular plane in opposite directions, were used for the CH_3 and C_2H_5, fragments, while only one was used for the H atom fragment. Four pivot points were used for the CH_2CHO and CH_3CHCHO fragments, placed on the reaction center and on the oxygen atom, above and below the molecular plane, and one on the CHO fragment, centered on the C atom. Two pivot points were used for CH_3CH_2CO, both placed on the plane of the carbon chain backbone in the direction of the breaking bond, on opposite sides of the radical carbon center. Pivot points centered on atoms were not shifted in the construction of the dividing surfaces, while those placed outside the molecular planes were displaced by 0.01, 0.3, and 0.5 bohrs perpendicularly to the plane. For R1, additional surfaces were constructed by placing the pivot points at 0.1 bohrs from the atomic centers. If multifaceted dividing surfaces were built, the total flux was estimated on a single face accounting for the symmetry of the dividing surfaces through the proper proportionality factor. In the case of R3, two pivot points were placed on the first fragment and shifted in opposite directions by 0.01, 0.3, and 0.5 bohr. However, the reactive flux was estimated only from the side of the multifaceted surface containing the radical center orbital, as the back side was considered as non reactive. Distances between the radical centers of the fragments were varied between 2.25 and 6 Å. For reaction R1, two repulsive potentials were added to the correction potential. The first one between the oxygen atom and the methyl carbon atom, to cancel the contribution of fluxes leading to CH_3 addition to O, and the second one between the ethyl radical center and the aldehydic hydrogen, in order to exclude the reaction flux leading to H abstraction. The use of repulsive potentials to eliminate the portions of the sampled reactive flux leading to unwanted reaction products is expected to have an impact on the simulation results similar to that obtained using multifaceted dividing surfaces and is necessary to cancel from the sampling performed on the spherical dividing surfaces the configurations that most likely lead to the formation of reaction products different from those studied. In the case of reaction R2, a repulsive potential was placed on the aldehydic hydrogen for the same reason. In addition to VRC-TST calculations, high pressure rate constants of the barrierless channels were also determined using VTST, which allowed to perform a comparison of the rate constants calculated at the two levels of theory.

All recombination rate constants were multiplied by flat correction factors of 0.9 to account for recrossing, as often done in VRC-TST calculations [53].

Phenomenological rate constants were determined using the MESS software and solving the multi-well 1D Master Equation (ME) over a PES consisting of reaction channels R1–R4 and R6 in the 300–2000 K and 0.1–100.0 atm temperature and pressure ranges, respectively. Collisional energy transfer parameters were computed as suggested by Jasper for a mixture with an Ar bath gas using the single exponential down model [55]. Since aldehydes are not included in the set of chemical species parameterized by Jasper, it was assumed by analogy that propanal and the corresponding alcohol, propanol, have a similar collisional energy

transfer behaviour. The downward energy transfer parameter so determined is $<\Delta E_{down}> = 397(T/300)^{0.52}$ cm^{-1}. The collisional frequency for C_2H_5CHO was estimated using a Lennard–Jones model with $\sigma = 4.14$ Å and $\varepsilon = 224.0$ K, also determined by analogy from the work of Jasper.

All DFT calculations were performed using Gaussian [56], while CCSD(T), MP2, and CASPT2 multireference energies were determined with Molpro [57]. Vibrational frequencies along the MEP were determined with EStokTP [50], which was also used to automate most of the calculation steps, such as conformational scans, 1DHR scans, determination of guesses for TSs, and evaluation of symmetry numbers. EStokTP also implements a protocol to prepare the inputs necessary for VTST and VRC-TST calculations.

2.2 Kinetic simulations

Kinetic simulations were performed in order to test the impact of the calculated rate parameters on the predictivity of existing kinetic mechanisms, in particular, focusing on the latest version of the CRECK mechanism [58]. For this purpose, the computed rate constants were fitted in the modified Arrhenius form $k = k_0 T^{\alpha} e^{-E_a/RT}$ (units mol, cm^3, s, cal) through nonlinear regression and expressed in CHEMKIN format. Pressure dependence was accounted for by fitting the rate constants determined through the ME integration at four different pressures, 0.1, 1.0, 10.0, and 100.0 atm in the PLOG format. Rate constants are reported in Section S1 of the Supplementary Information (SI). The latest version of the CRECK mechanism contains the reactions of dissociation of propanal to C_2H_5 (R1) and CH_3 (R2), and their reverse rates ($R1_B$, $R2_B$), computed through detailed balance. In the present work the rate constants of these reactions were updated with the computed estimates, while R3, R4, and the termolecular R6 reaction were added to the mechanism. The original and modified kinetic mechanisms were used to simulate the shock tube experimental studies of the pyrolysis of 3% propanal in Ar performed by Pelucchi et al. [19] and 1% propanal in Ar performed by Lifshitz [18] using the OpenSMOKE++ suite of programs [59]. Simulations were performed with the latest release of the CRECK mechanism [58] (CRECK 20_03, March 2020 version), in its original version and modified through the inclusion of the reaction rates estimated in this work. The CRECK 20_03 kinetic mechanism, formulated so that it is apt to describe high temperature (HT) pyrolysis and combustion of C_1–C_3 species, consists of 114 species and 1999 reactions prior to modifications. It should be noted that the shock tube simulations were performed using a non isothermal model, as implemented in OpenSMOKE++, which is able to properly account for temperature changes with conversion that can be determined by the reaction endothermicity.

3 Results

3.1 Potential energy surface

The PES used to describe the propanal decomposition mechanism is shown in Fig. 1. It reports high level CCSD(T)/CBS reaction energies computed as described in the method section with respect to the reactant well, C_2H_5CHO. A summary of the reaction energies computed in this work, previous literature estimates, and the ATcT values is reported in Tables 1 and 2 for values at 0 and 298.15 K, respectively.

It can be noticed that the 0 K energy changes of R1 and R2 in this work are close, differing by just 0.2 kcal/mol, with the channel leading to $C_2H_5 + CHO$ being energetically favoured. This opens up the interesting question about which channel is going to be the fastest at equal reaction endothermicity. While the energy changes calculated in the present work are in excellent agreement with the ATcT values, from which they differ by less than 0.2 kcal/mol, a difference can be observed with previous literature estimates. In particular, it is found that the reaction energy changes computed by Chin and Lee [35] at the CCSD(T)/6–311 + G(3df,2p)//B3LYP/6-311G(d,p) level differ by the ATcT values by more than 1 kcal/mol. Leonori et al. [42] used an extrapolation to the CBS limit from the aug-cc-pVDZ and aug-cc-pVTZ basis sets, finding a maximum error of 0.9 kcal/mol. Part of it is due to neglecting core electron correlation, which accounts for about 0.2 kcal/mol for the $C_2H_5CHO \rightarrow CHO + C_2H_5$ reaction energy change. The

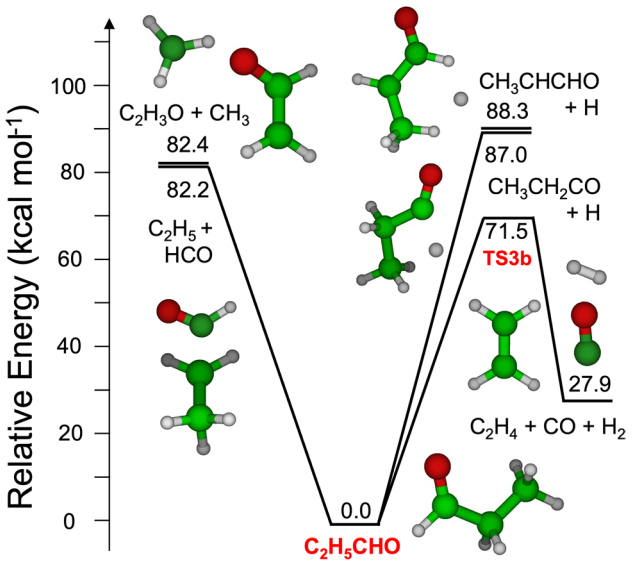

Fig. 1 Portion of the propanal PES investigated in this work, containing all the reaction channels found to contribute significantly to the decomposition mechanism: four barrierless dissociation channels and the three-body dissociation (TS3b) to $C_2H_4 + CO + H_2$

Table 1 Comparison of calculated bond dissociation enthalpies [kcal/mol] at 0 K, inclusive of ZPE corrections, with literature estimates from Leonori et al. [42], Chin and Lee [34], Klippenstein et al. [61] and ATcT [62] reference values. Missing ATcT values indicate the absence from the database of at least a species involved in the reaction

Reaction channel $C_2H_5CHO\rightarrow$	This work[a]	Leonori[b]	Chin[c]	Klippenstein[d]	ATcT
CH_3CH_2+CHO (R1)	82.2	81.6	80.6	81.8	82.17 ± 0.13
$CH_2CHO+CH3$ (R2)	82.4	81.3	81.1	82.1	82.21 ± 0.21
CH_3CH_2CO+H (R3)	88		86.1	88.2	
$CH_3CHCHO+H$ (R4)	89.3			89	
CH_2CH_2CHO+H (R5)	100.3			100.3	
$CO+C_2H_4+H_2$ (R6)	27.9	27.9	26.7	27.9	28.26 ± 0.09

[a]0 K—[a]CCSD(T)/CBS + core energies on ωB97X-D/aug-cc-pVTZ structures

[b]0 K—CCSD(T)/CBS or CASPT2/aug-cc-pVTZ energies on CASPT2/aug-cc-pVTZ structures

[c]0 K—CCSD(T)/6–311 + G(3df,2p) energies on B3LYP/6-311G(d,p) structures

[d]0 K—ANL0 method

Table 2 Comparison of literature bond dissociation enthalpies [kcal/mol] at 298.15 K from da Silva and Bozzelli [60], Pelucchi et al. [19] and ATcT [62] reference values. Missing ATcT values indicate the absence from the database of at least a species involved in the reaction

Reaction channel $C_2H_5CHO\rightarrow$	ATcT	da Silva[a]	Pelucchi[b]
CH_3CH_2+CHO (R1)	83.37 ± 0.13	83.8	84.4
$CH_2CHO+CH_3$ (R2)	83.45 ± 0.21	83.7	83.5
CH_3CH_2CO+H (R3)		89.3	89
$CH_3CHCHO+H$ (R4)		90.2	91.9
CH_2CH_2CHO+H (R5)		102.4	
$CO+C_2H_4+H_2$ (R6)	30.69 ± 0.09		

[a]298 K—CBS-APNO method

[b]298 K—evaluation of bond dissociation energies by analogy

remaining 0.4 kcal/mol of difference with respect to the present calculations can be explained by the use of smaller basis sets for the CBS extrapolation. Despite the difference in the theoretical estimates of 0 K bond enthalpies for R1 and R2 performed at different theoretical levels, it is though interesting to notice that all calculations are in reasonable agreement with experimental data. This holds true also for the computations performed by da Silva and Bozzelli [60] and Pelucchi et al. [19] at 298 K, where the calculated endothermicity of the reactions only slightly exceeds the ATcT reference enthalpies. The enthalpy difference between R1 and R2 is the largest in the work of Pelucchi et al. (i.e., 1 kcal/mol), which can be explained by the fact that bond energies were computed using an analogy-based group additivity method.

The relative strengths of the C–H bonds indicate that the aldehydic H loss is favoured among the H loss channels, as found also by da Silva and Bozzelli [60] and Pelucchi et al. [19]. The calculations of Chin and Lee [35] underestimate the present theoretical estimate by about 2 kcal/mol. It can also be noticed that the reaction endothermicity for H loss from the C2 carbon atom is similar, differing only by 1.3 kcal/mol. The C–H bond dissociation enthalpy for H loss from the terminal methyl group was computed as well and it was found, as expected, that the energy change for this reaction channel (R5) is considerably higher. The calculated value of 100.3 kcal/mol is indeed in line with bond enthalpies of primary hydrogen atoms found in hydrocarbons [9]. The high endothermicity of the R5 channel is the reason why it was not included among the investigated propanal reaction pathways.

The concerted decomposition reaction to form $CO+C_2H_4+H_2$ (R6) was included among the main pathways contributing to propanal decomposition since, as found in previous literature studies [35, 42], it is the channel with the lowest energy barrier among those that proceed through a saddle point. Therefore, though entropically unfavoured with respect to bond scission reactions, it is likely to contribute significantly to the reactivity at low temperatures. It is interesting to compare the 0 K bond enthalpies computed in this work with the enthalpies calculated using the thermochemical database by Klippenstein et al. [61], who determined 0 K enthalpies of formation for 348 hydrocarbons, oxygenated, and nitrogen containing species relevant in combustion systems, at the very accurate ANL0 level of theory. The endothermicity of R1 and R2 is once more found to be similar, with R2 being slightly more endothermic (0.3 kcal/mol against the 0.2 kcal/mol from this work). The ANL0 database reports additional data with respect to the ATcT [62], which allowed us to compare the bond enthalpies of R3, R4, R5, and R6 calculated in this work with the ANL0 estimates. The agreement between the two sets of calculations is quite good, and it is interesting to notice that all bond enthalpies from this work differ by less than 0.4 kcal/mol with respect to the results obtained with the ANL0 method.

3.2 Barrierless channels

The MEP potentials calculated for the four barrierless reaction channels investigated in this work are reported in Fig. 2. Each potential was estimated at two different levels of theory. At the highest, energies are computed at the CASPT2(4e,4o)/aug-cc-pVTZ (atz) level on geometries optimized at fixed lengths of the breaking bond at the CASPT2(4e,4o)/jun-cc-pVTZ level. At the lowest, energies are computed at the CASPT2(2e,2o)/cc-pVDZ (dz) level on the geometries used for the successive VRC-TST stochastic sampling.

All the reported MEP potentials do not include ZPE corrections. Regarding R2, the MEP built with a larger (10e,9o) active space was also reported to show the limited influence of the size of the active space in the calculations. It is observed that the MEP profiles with an atz basis set computed with the two active spaces are almost superimposed when the fragment separation is above 3 Å. Below this threshold, the larger active space is more attractive, which leads to a slight decrease of the correction potential. In all cases, it is found that the CASPT2(2e,2o)/dz MEP potential underestimates the interaction between the fragments. This is accounted for in the VaReCoF implementation of VRC-TST through a correction potential, whose geometric and energetic contributions are reported in Fig. 3.

The energy correction term of the correction potential originates from the difference between the high level energies computed with a larger basis set and active space and the energies calculated at the level of theory used for the VRC-TST stochastic sampling. The geometry relaxation term of the correction potential stems from the use of fixed fragments geometries in the stochastic sampling and hence it accounts for the energy gained for fragments relaxation along the MEP. The geometry correction term shown in Fig. 3 generally decreases at lower fragments separation, but this is not the case for R3. Comparing the loss of the H atom from the carbonyl group (R3) and the central carbon (R4), the latter involves a change of hybridization of the formed CH_3CHCHO radical from sp^3 to sp^2, which leads to a greater geometry contribution to the correction potential as the fragments are brought closer to each other. On the other hand, the separation of the H atom from the CH_3CH_2CO radical does not imply a major conformational change, so that at low

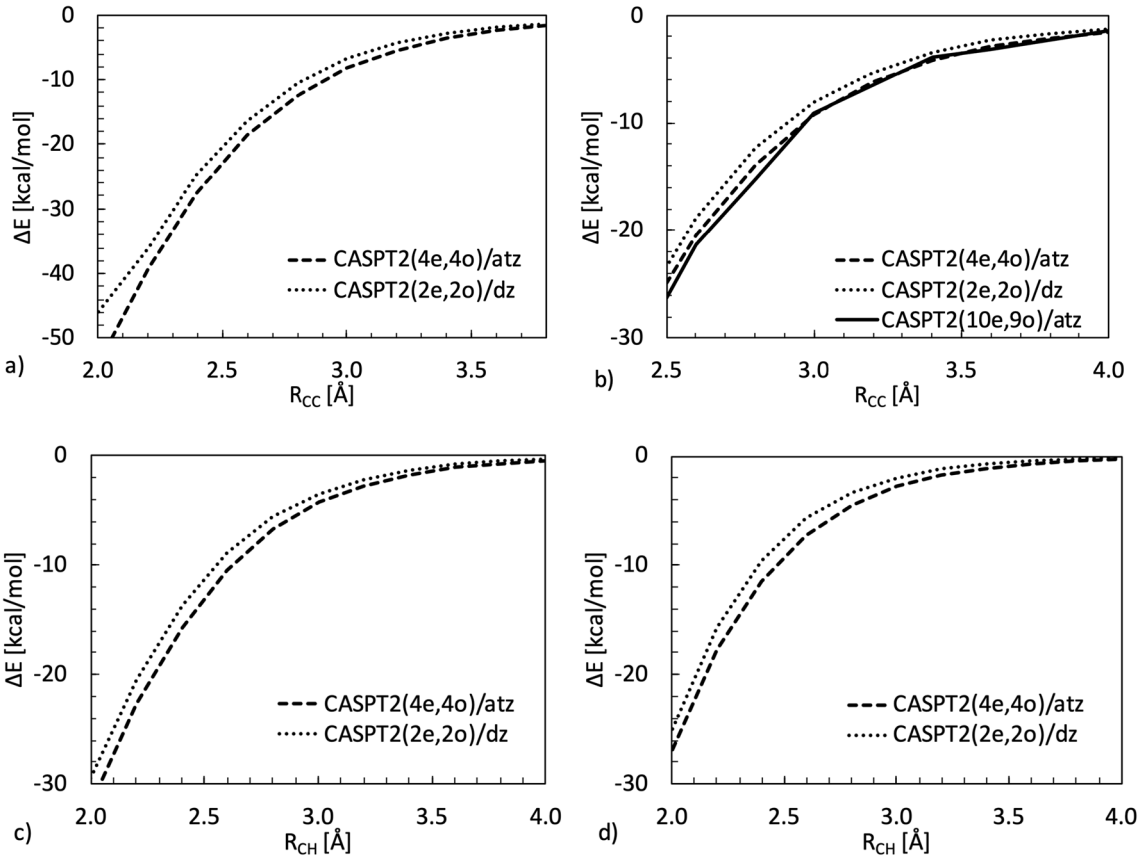

Fig. 2 MEP potentials for propanal decomposition reactions leading to **a** CH_3CH_2+CHO (R1), **b** CH_3+CH_2CHO (R2), **c** CH_3CH_2CO+H (R3), and **d** $CH_3CHCHO+H$ (R4) calculated at the CASPT2(4e,4o)/aug-cc-pVTZ (dashed) and CASPT2(2e,2o)/cc-pVDZ (dotted) levels. The MEP for R2 was also determined using the (10e,9o) active space (solid)

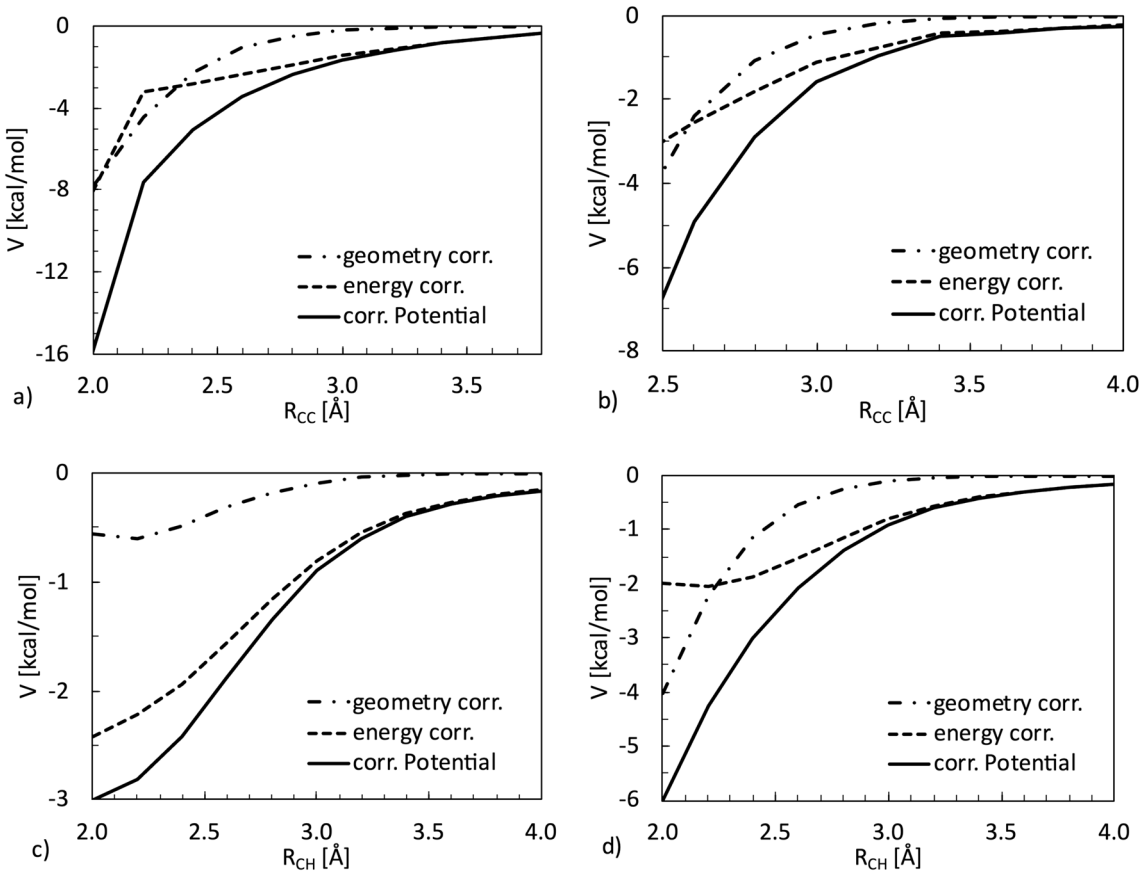

Fig. 3 Correction potential (solid) and its geometry (dash-dot) and energy (dashed) contributions for reactions leading to **a** CH_3CH_2+CHO (R1), **b** CH_3+CH_2CHO (R2), **c** CH_3CH_2CO+H (R3) and **d** $CH_3CHCHO+H$ (R4)

fragments separation the energy difference between relaxed and constrained geometries does not decrease systematically. The energy contribution shows a similar trend, decreasing at lower fragments distance. For R4, it reaches an almost constant value below 2.4 Å. The energetic correction is always the dominant contribution to the correction potential above 3 Å. All MEP and correction potential calculations for R2 were performed only above 2.4 Å, as the molecular configuration along the MEP changes significantly below this threshold, since the methyl radical orientation with respect to the CH_2CHO fragment changes from in plane to out of plane relatively to the CCHO backbone.

While the experimental estimation of decomposition rates is complicated by the need of accounting for secondary reactivity, the determination of elementary rate constants for the inverse recombination processes can be performed in temperature and pressure conditions where their impact is negligible. Thus, experimental data for radical recombination reactions forming aldehydes is available in the literature for reaction $R1_B$. This type of study usually exploits photodissociation of the parent molecule. An example is the work of Zhu et al. [63], who post-processed the time dependent profiles of the radicals generated via photolysis at 293 ± 2 K and 3 torr of propanal partial pressure in the 280–330 nm region to estimate the rate constants of three recombination reactions. These included formyl and ethyl recombination to propanal, for which a rate constant of $k_{R1B} = 6.5 \pm 1.5 \times 10^{-11}$ cm^3/s was reported. Baggot et al. [64] studied the photolysis of five C_2–C_4 aldehydes at 308 nm, by using both end-product analysis and time-resolved techniques. They monitored the concentration of CHO over time following flash photolysis at 297 ± 2 K. Rate constants were determined for different recombination reactions, including the recombination of formyl and ethyl radicals: $k_{R1B} = 7.2 \pm 1.6 \times 10^{-11}$ cm^3/s. Results from theoretical calculations are compared with experimental values in Fig. 4, showing, in the case of VRC-TST, an excellent agreement (i.e., $< 20\%$).

The high pressure recombination rate constants calculated in this work in the 300–2000 K temperature range are reported in Fig. 5. It can be observed that, as expected, H atom recombination reactions are the fastest. There is though a significant difference in the computed temperature dependence, with H recombination on the aldehydic carbon the fastest and almost temperature independent, while

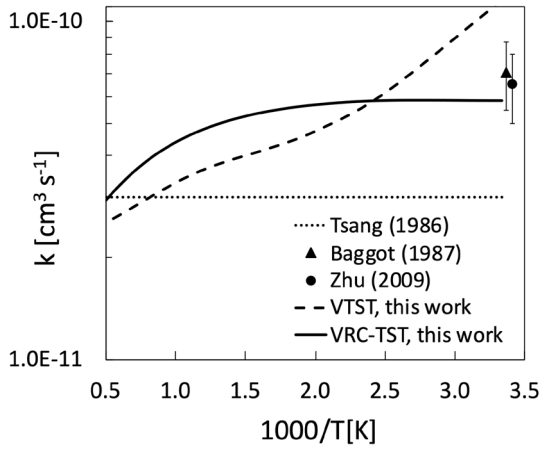

Fig. 4 Comparison between the $R1_B$ rate constant ($C_2H_5 + CHO \rightarrow C_2H_5CHO$) as evaluated with VTST (dashed) and VRC-TST (solid), experimentally measured by Baggot [64] and Zhu [63], and recommended by Tsang [66] (dotted)

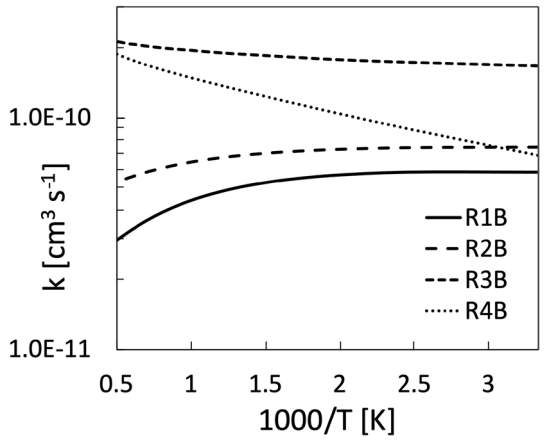

Fig. 5 High pressure recombination rate constants reported as a function of the inverse of temperature in the 300–2000 K range for the investigated reaction channels

the recombination rate on the secondary carbon radical site increases almost by a factor of three between 300 and 2000 K. Such a high temperature dependence is rarely observed in H recombination reactions (see for example [65]), and it may be determined by the fact that in the calculations the competitive H recombination channel on the oxygen atom, leading to the formation of the enol adduct, has not been considered. This may lead to a decrease of the low temperature reactive flux, as the multifaceted dividing surface for the two reactive channels, being farther from the reactive centers, may partially overlap and have similar potential, thus becoming a competitive reaction channel. On the other side, the recombination of formyl ($R1_B$) and methyl radicals ($R2_B$) with the respective co-products shows an inverse trend, slowing down as the temperature increases. The HPL rate constants for the investigated recombination reactions are reported in the SI.

It is worth to focus on the $R1_B$ reaction, namely the recombination of C_2H_5 and CHO, for which experimental data are available at room temperature as anticipated in Fig. 4. In addition to the experimental values [63, 64] the recommendation by Tsang and Hampson [66] is also reported in Fig. 4 together with the results from the present ME simulations, performed using both VRC-TST and VTST theories. It can be noted that the rate constant computed with VRC-TST is in good agreement with experimental data, which are overestimated by VTST by about a factor of 2 at 300 K. As the temperature increases, the VTST and VRC-TST rate constants become similar, differing by just 10% at 2000 K. The loss of accuracy observed for VTST at low temperatures can be explained in terms of the loss of accuracy of the harmonic approximation used to compute the density of states along the MEP in VTST. In fact, as the temperature decreases the dividing surface position moves to larger fragment separation, where the attractive potential is small. In these conditions, the Rigid Rotor Harmonic Oscillator approximation used in VTST fails to describe properly the large amplitude motions of the transitional degrees of freedom describing the relative orientation of the two fragments.

3.3 Propanal decomposition mechanism and rate constants

Phenomenological rate constants for the five decomposition rate channels of propanal here investigated were determined through the integration of the one-dimensional ME in the 0.1–100 atm and 300–2000 K pressure and temperature ranges, respectively. As expected, and in agreement with previous literature studies performed for this system [19], the dominant reaction is R1, closely followed by R2 above 1000 K at all the considered pressures. The channel specific rate constants computed in the 900–1400 K temperature range at the HPL are compared in Fig. 6a. This is the temperature range where the decomposition of propanal has been experimentally measured [19] and in which the kinetic simulations described in Sect. 3.4 were performed. It can be noted that the contribution of the 3-body dissociation pathway is heavily influenced by the temperature: it plays a minor role at high temperature, but it approaches and surpasses R2 at low temperature. The H loss channels R3 and R4 are significantly slower than the other dissociation channels at all conditions; at 2000 K they are more than 2 orders of magnitude slower with respect to R1, and the difference grows as the temperature decreases. The pressure-dependent PLOG Arrhenius equation parameters, computed at 0.1, 1.0, 10.0, and 100.0 atm are reported in the SI, while the

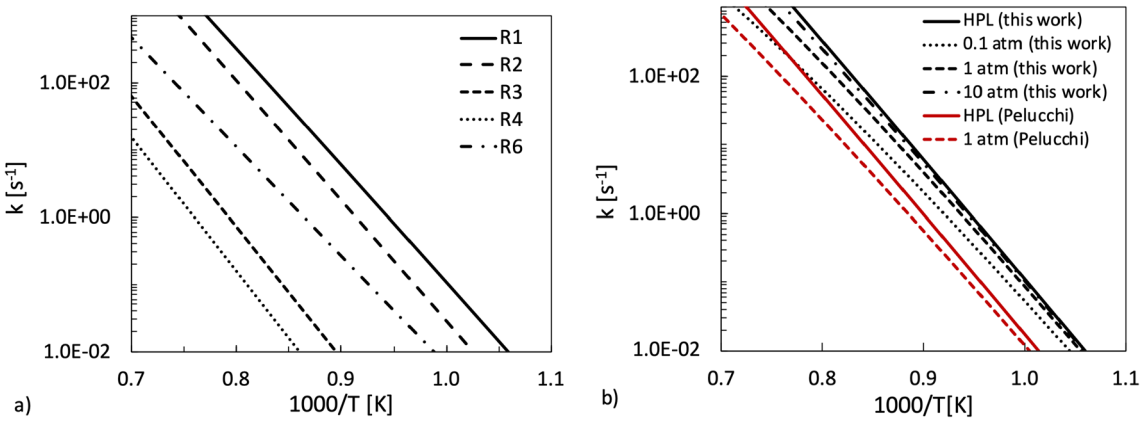

Fig. 6 **a** HPL rate constants for the five fastest decomposition reactions of propanal. **b** Comparison of the R1 rate constant with that estimated through analogy by Pelucchi et al. [19] at different pressures

modified Arrhenius equation parameters for the HPL rate constants, interpolated between 400 K and 2000 K, (with R expressed in kcal/mol/K and T in K) are:

$$k_{R1} = 2.19 \text{ x } 10^{25} T^{-2.58} exp\left(-\frac{85.0}{RT}\right)\left[\frac{1}{s}\right]$$

$$k_{R2} = 9.33 \text{ x } 10^{20} T^{-1.34} exp\left(-\frac{84.6}{RT}\right)\left[\frac{1}{s}\right]$$

$$k_{R3} = 1.17 \text{ x } 10^{17} T^{-0.47} exp\left(-\frac{90.1}{RT}\right)\left[\frac{1}{s}\right]$$

$$k_{R4} = 3.63 \text{ x } 10^{14} T^{0.16} exp\left(-\frac{90.7}{RT}\right)\left[\frac{1}{s}\right]$$

$$k_{R6} = 5.62 \text{ x } 10^{7} T^{1.78} exp\left(-\frac{70.0}{RT}\right)\left[\frac{1}{s}\right]$$

The rate constants from Pelucchi et al. [19] and those computed in the present work at the HPL and 1 atm for reaction R1 are compared in Fig. 6b. Fall off effects are present in both studies, and it can be noted that the rate constants from the literature are around one order of magnitude slower both at 1 atm and at the HPL when compared to those computed in the present study. This is expected to affect the outcome of kinetic simulations of propanal decomposition, given that R1 is its main decomposition pathway. A more detailed comparison of the R1 rate constant computed in this work and that reported in the CRECK 2015 mechanism in the 300–2000 K temperature range at the HPL is available in the SI. The branching fractions (BF) among the main reaction channels are summarized in Table 3 at the HPL, as they are only slightly affected by the pressure. It can be noted how the molecular channel R6 is dominant at low temperatures, while R1 becomes the fastest reaction above 1000 K, accounting for about 76% of the system reactivity. R2 contribution is also important, accounting for about 24% of the system reactivity up to 2000 K. The R6 reaction channel is dominant below 600 K at all the considered pressures.

3.4 Kinetic simulations

The shock tube experiments of the pyrolysis of 3% C_2H_5CHO in Ar by Pelucchi et al. [19] were simulated with the intent of investigating the impact on propanal reactivity of the calculated decomposition rate constants. For the experimental concentrations of small hydrocarbons measured in the post-shock mixtures, uncertainties lower than 2% were reported, while the estimated uncertainty for propanal was less than 8%. Simulations were performed in the 900–1500 K temperature range at 1.8 atm following the approach described in Sect. 2.2. Figure 7 compares the experimental data, the simulations results of Pelucchi et al. [19] (CRECK 15_02), and the results obtained with the current release version of the CRECK mechanism as it is (CRECK 20_03) [58] and updated with the rate constants from this study (CRECK 20_03mod). The concentration profiles of C_2H_5CHO, CO, C_2H_2, C_2H_4, C_2H_6, and C_3H_8 were normalized over the initial propanal concentration and are reported in Fig. 7 as a function of the inlet mixture

Table 3 Branching fractions computed at the high pressure limit as a function of temperature for the dominant reaction channels (R1, R2, and R6)

T[K]	R6	R1	R2
500	0.83	0.15	0.02
1000	0.05	0.76	0.19
1500	0.03	0.75	0.22
2000	0.02	0.74	0.24

temperature. Furthermore, normalized concentration profiles of CH_4 and C_3H_6 were reported in the SI.

It can be noted that both the CRECK 15_02 and CRECK 20_03 models underestimate the decomposition of propanal (Fig. 7a). A better agreement with the experiments though is observed using the CRECK 20_03mod mechanism. Indeed, the propanal conversion increases by 8% at 1120 K and 37% at 1340 K with respect to what predicted by the CRECK 20_03 model. This difference is consistent with the fact that the rate constant calculated in this work for the fastest decomposition reaction, R1, is one order of magnitude higher than that used in both the CRECK 15_02 and CRECK 20_03 mechanisms. The comparison of the R1 (and R2) rate constants computed in this work and in the literature [19] at the HPL is reported in the SI. Both experiments and simulations show that the onset of propanal decomposition is at around 1050 K. The CRECK 15_02 and CRECK 20_03 models underestimate the formation of CO (Fig. 7b), which is more accurately predicted by the CRECK 20_03mod model. This is compatible with the higher consumption of propanal predicted by the latter mechanism, which in turn leads to a higher concentration of the main pyrolysis product, CO. Similar considerations apply to other relevant molecular products, such as C_2H_2 (Fig. 7c) and C_2H_4 (Fig. 7d). Also in the cases of C_2H_6 (Fig. 7e) and C_3H_8 (Fig. 7f), differences are noticeable between the CRECK 20_03mod results and the other mechanisms, with the former providing a more accurate reproduction of the experimental results, especially between 1100 and 1300 K. Analogous trends were observed comparing the results of the three models with the shock tube experiments of Lifshitz et al. [18] of the pyrolysis of 1% propanal in Ar. The comparison between the predicted and experimental concentration profiles are reported in the SI.

In order to determine which are the main reaction pathways a sensitivity analysis was performed for propanal decomposition at 1300 K. The results, reported in Fig. 8, show that both R1 and R2 are among the most sensitive reactions, indicating that propanal is mostly influenced by the unimolecular decomposition to ethyl and formyl radicals (R1), followed by ethyl decomposition to ethylene and hydrogen ($C_2H_5 = H + C_2H_4$). Other important reactions, that present a negative sensitivity coefficient and thus contribute to propanal consumption, are H abstraction from C_2H_5CHO, its isomerization to propenol, H abstraction from ethyl followed by decomposition to C_2H_5 and CO, and the decomposition reaction R2, leading to methyl and CH_2CHO. Focusing on channels that show a positive sensitivity coefficient, i.e. that inhibit reactivity, it is interesting to notice the role of the ethyl radical self recombination reaction ($C_2H_5 + C_2H_5 = C_4H_{10}$), which acts as a sink of ethyl radicals, thus decreasing the reactivity compared

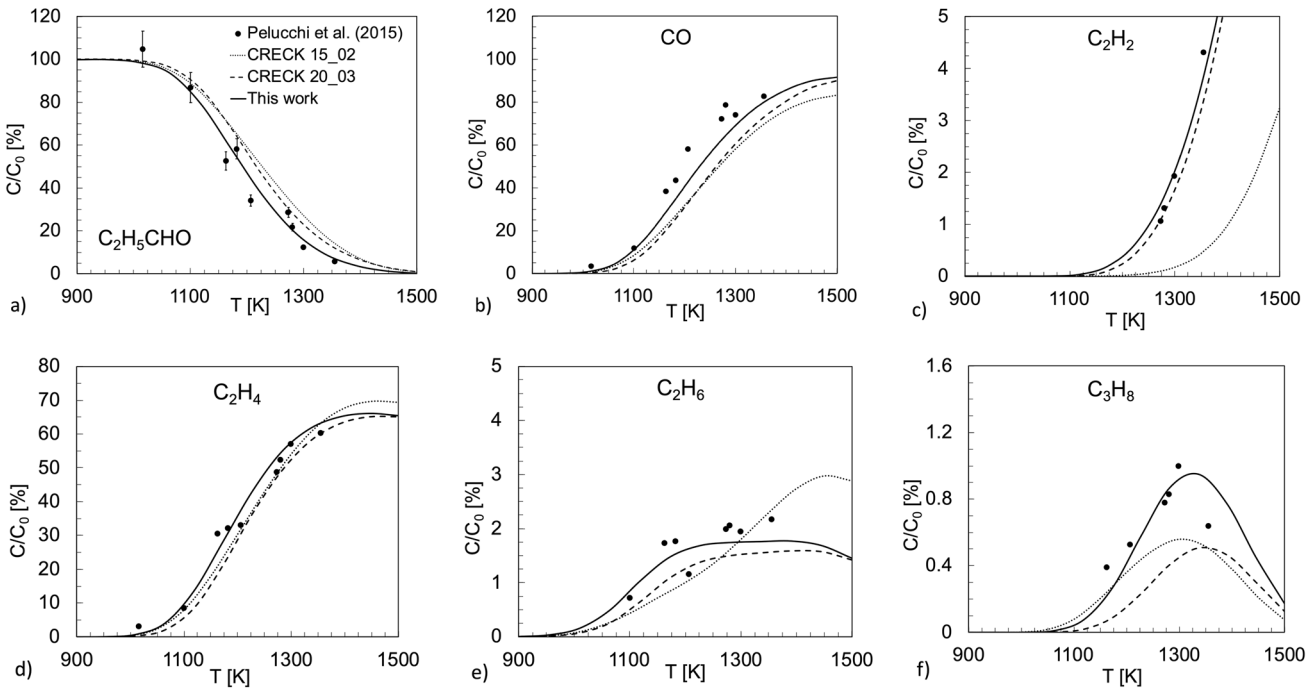

Fig. 7 Predicted concentration profiles from the shock tube pyrolysis of 3% propanal in Ar in the 900–1500 K temperature range at 1.8 atm. Both experimental data and simulations (residence time 2.5 ms) with three different mechanisms, namely CRECK 15_02 (dotted line), CRECK 20_03 (dashed) and CRECK 20_03mod (solid) are reported. **a** C_2H_5CHO, **b** CO, **c** C_2H_2, **d** C_2H_4, **e** C_2H_6, and **f** C_3H_8 concentrations were normalized over the initial reactant concentration C_0

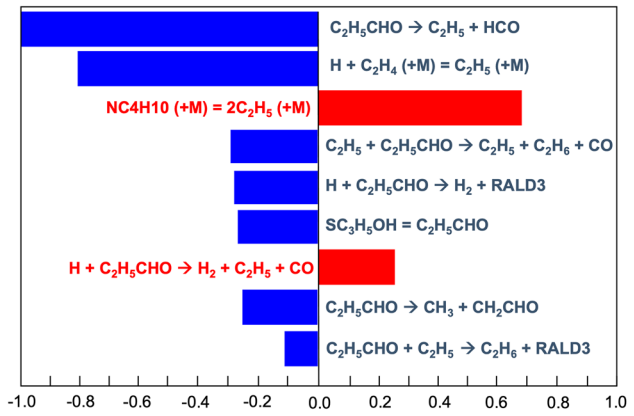

Fig. 8 Sensitivity analysis performed for propanal decomposition at 1300 K. The sensitivity coefficients were normalized with respect to the decomposition of propanal to formyl and ethyl radicals

to the propagation channel $C_2H_5 = H + C_2H_4$. Overall, the ethyl radical chemistry onset, initiated by the dominating decomposition reaction R1, governs propanal reactivity in the high temperature pyrolysis conditions.

Finally, additional simulations were performed in order to test the impact of the shock tube effective reaction time on the simulations results and how the sensitivity analysis changes with temperature. In particular, the effective reaction time was varied between 0.002 s and 0.003 s, while the sensitivity analysis for propanal decomposition was performed also at 1150 K, thus at lower propanal conversion. The results, reported in the SI, show that both kinetic simulations and sensitivity analysis are not influenced by these changes.

4 Conclusions

This study investigated the unimolecular decomposition mechanism of propanal, determining channel specific temperature and pressure dependent rate constants using state of the art theoretical methods. It was found that propanal decomposition is controlled by four barrierless decomposition pathways and one molecular channel. The comparison between calculated and available experimental reaction energy changes showed a remarkable agreement, with a maximum difference of 0.3 kcal/mol. The fastest decomposition channels lead to the formation of the ethyl and formyl radicals (R1), followed by the methyl and vinoxy radicals at temperatures higher than 600 K. As the temperature decreases below 600 K the main channel becomes the molecular decomposition to ethane, CO, and hydrogen.

The calculated bimolecular high pressure rate constants for barrierless recombination reactions are in quantitative agreement with the experimental measurement for the $HCO + C_2H_5$ recombination channel ($R1_B$), thus increasing confidence in the rate constants estimations of the inverse unimolecular decomposition channels, for which no direct experimental measurements are available. Notably, both the high pressure and pressure dependent computed decomposition rate constants differ by about a factor of 10 from the rate constants presently included in reference literature kinetic mechanisms [58]. A theoretical assessment of the impact of using VRC-TST and VTST for the estimation of rate constants for barrierless reactions for the $HCO + C_2H_5$ channel was also provided in this study. It was found that at low temperatures the VTST rate constant is twice as fast as the VRC-TST prediction, which is in quantitative agreement with experimental data. Increasing the temperature leads to better consistency between the two approaches, which are in good agreement at 2000 K. While the good performance of VRC-TST was expected, there is much less evidence that reasonable predictions can be obtained using VTST. In this regard, it is likely that relatively good predictions were obtained with VTST in this work as Hessians, and thus harmonic frequencies, were determined using the CASPT2 multireference approach with a relatively large basis set (aug-cc-pVTZ), treating anharmonic torsional frequencies as hindered rotors. The accuracy of this approach is expected to be reasonable when the minimum of the reacting flux is located at short fragment separations, as is the case for high temperature conditions, and thus when the relative motions of the molecular fragments can be properly described with a harmonic model.

Finally, to test the impact of the updated reaction mechanism for propanal decomposition on the prediction of its reactivity, kinetic simulations of shock tube pyrolysis data from the literature were performed. It was found that the new set of rate constants leads to an improved agreement with experimental decomposition profiles, intermediates, and products formation. The temperature and pressure dependent calculated rate constants are reported in the SI for implementation in other kinetic models. We believe that the current results constitute an important reference for future kinetic investigation of propanal reactivity, as well as for the re-estimation of the decomposition rate constant of larger aldehydes. It is in fact likely that the rate parameters presently included in existing kinetic mechanisms are underestimated, as they were determined using the same approach, based on

analogy rules, that we found to significantly underestimate propanal decomposition rates.

5 Supplementary Information

The supplementary information contains the following information, available free of charge:

- All the input files necessary to run the 1D multiwell ME simulation as a zip file. These include the MESS text input file and the text files containing the VRC-TST reactive fluxes.
- The rate constants derived in this study, reported in PLOG Chemkin format, the comparison of the HPL recombination rate constants over the 300–2000 K temperature range, and the comparison of R1 and R2 HPL rate constants against the one reported by Pelucchi et al. [19] and employed in the CRECK kinetic model.

Supplementary Information The online version contains supplementary material available at https://doi.org/10.1007/s00214-023-03060-2.

Acknowledgements This work has been supported by the Italian MUR (PRIN 2017—Grant 2017PJ5XXX, and PRIN 2020—Grant 202082CE3T). The authors acknowledge the CINECA award HP10BCGTXF, under the ISCRA initiative, for the availability of high performance computing resources and support.

Author contributions A. D. and M. D. performed the quantum-chemical and kinetic computations and analyzed the results; C.C. conceived the computational strategy and coordinated the interpretation of its results; M.P. supervised the kinetic simulations; A.D., M.D., M.P., and C.C. co-wrote the paper. All authors discussed the results and commented on the manuscript.

Funding Open access funding provided by Politecnico di Milano within the CRUI-CARE Agreement.

Declarations

Conflict of interests The authors declare no competing interests.

References

1. Hollis JM, Jewell PR, Lovas FJ, Remijan A, Møllendal H (2004) Green bank telescope detection of new interstellar aldehydes: propenal and propanal. Astrophys J 610:L21–L24. https://doi.org/10.1086/423200
2. Singh SK, Fabian Kleimeier N, Eckhardt AK, Kaiser RI (2022) A mechanistic study on the formation of Acetone (CH_3COCH_3), Propanal (CH_3CH_2CHO), Propylene Oxide (c-CH_3CHOCH_2) along with their propenol enols ($CH_3CHCHOH/CH_3C(OH)CH_2$) in interstellar analog ices. Astrophys J 941:103. https://doi.org/10.3847/1538-4357/ac8c92
3. Cavaliere A, Ciajolo A, D'Anna A, Mercogliano R, Ragucci R (1993) Autoignition of n-heptane and n-tetradecane in engine-like conditions. Combust Flame 93:279–286. https://doi.org/10.1016/0010-2180(93)90109-G
4. Burluka AA, Harker M, Osman H, Sheppard CGW, Konnov AA (2010) Laminar burning velocities of three C_3H_6O isomers at atmospheric pressure. Fuel 89:2864–2872. https://doi.org/10.1016/j.fuel.2010.02.004
5. Grosjean D, Grosjean E, Gertler AW (2001) On-road emissions of carbonyls from light-duty and heavy-duty vehicles. Environ Sci Technol 35:45–53. https://doi.org/10.1021/es001326a
6. Poulopoulos SG, Samaras DP, Philippopoulos CJ (2001) Regulated and unregulated emissions from an internal combustion engine operating on ethanol-containing fuels. Atmos Environ 35:4399–4406. https://doi.org/10.1016/S1352-2310(01)00248-5
7. He P-J, Tang J-F, Yang N, Fang J-J, He X, Shao L-M (2012) The emission patterns of volatile organic compounds during aerobic biotreatment of municipal solid waste using continuous and intermittent aeration. J Air Waste Manag Assoc 62:461–470. https://doi.org/10.1080/10962247.2012.658954
8. Pang X, Shi X, Mu Y, He H, Shuai S, Chen H, Li R (2006) Characteristics of carbonyl compounds emission from a diesel-engine using biodiesel–ethanol–diesel as fuel. Atmos Environ 40:7057–7065. https://doi.org/10.1016/j.atmosenv.2006.06.010
9. Pelucchi M, Cavallotti C, Ranzi E, Frassoldati A, Faravelli T (2016) Relative reactivity of oxygenated fuels: alcohols, aldehydes, ketones, and methyl esters. Energy Fuels 30:8665–8679. https://doi.org/10.1021/acs.energyfuels.6b01171
10. Frassoldati A, Cuoci A, Faravelli T, Niemann U, Ranzi E, Seiser R, Seshadri K (2010) An experimental and kinetic modeling study of n-propanol and iso-propanol combustion. Combust Flame 157:2–16. https://doi.org/10.1016/j.combustflame.2009.09.002
11. Capriolo G, Konnov AA (2020) Combustion of propanol isomers: experimental and kinetic modeling study. Combust Flame 218:189–204. https://doi.org/10.1016/j.combustflame.2020.05.012
12. Man X, Tang C, Zhang J, Zhang Y, Pan L, Huang Z, Law CK (2014) An experimental and kinetic modeling study of n-propanol and i-propanol ignition at high temperatures. Combust Flame 161:644–656. https://doi.org/10.1016/j.combustflame.2013.08.003
13. Akih-Kumgeh B, Bergthorson JM (2011) Ignition of C3 oxygenated hydrocarbons and chemical kinetic modeling of propanal oxidation. Combust Flame 158:1877–1889. https://doi.org/10.1016/j.combustflame.2011.02.015
14. Yang K, Zhan C, Man X, Guan L, Huang Z, Tang C (2016) Shock tube study on propanal ignition and the comparison to Propane, *n*-Propanol, and *i*-Propanol. Energy Fuels 30:717–724. https://doi.org/10.1021/acs.energyfuels.5b02739

15. Kohse-Höinghaus K, Oßwald P, Cool TA, Kasper T, Hansen N, Qi F, Westbrook CK, Westmoreland PR (2010) Biofuel combustion chemistry: from ethanol to biodiesel. Angew Chem Int Ed 49:3572–3597. https://doi.org/10.1002/anie.200905335
16. Veloo PS, Dagaut P, Togbe C, Dayma G, Sarathy SM, Westbrook CK, Egolfopoulos FN (2013) Jet-stirred reactor and flame studies of propanal oxidation. Proc Combust Inst 34:599–606. https://doi.org/10.1016/j.proci.2012.06.138
17. Kasper T, Struckmeier U, Oßwald P, Kohse-Höinghaus K (2009) Structure of a stoichiometric propanal flame at low pressure. Proc Combust Inst 32:1285–1292. https://doi.org/10.1016/j.proci.2008.06.040
18. Lifshitz A, Tamburu C, Suslensky A (1990) Decomposition of propanal at elevated temperatures: experimental and modeling study. J Phys Chem 94:2966–2972. https://doi.org/10.1021/j100370a043
19. Pelucchi M, Somers KP, Yasunaga K, Burke U, Frassoldati A, Ranzi E, Curran HJ, Faravelli T (2015) An experimental and kinetic modeling study of the pyrolysis and oxidation of n-C_3C_5 aldehydes in shock tubes. Combust Flame 162:265–286. https://doi.org/10.1016/j.combustflame.2014.07.027
20. Dias V, Vandooren J, Jeanmart H (2016) Experimental and modeling study of Propanal/H_2/O_2/Ar flames at low pressure. Combust Sci Technol 188:556–570. https://doi.org/10.1080/00102202.2016.1145017
21. Barari G, Koroglu B, Masunov AE, Vasu S (2017) Products and pathways of aldehydes oxidation in the negative temperature coefficient region. J of Energy Resour Technol 139:012203. https://doi.org/10.1115/1.4033589
22. Capriolo G, Alekseev VA, Konnov AA (2018) An experimental and kinetic study of propanal oxidation. Combust Flame 197:11–21. https://doi.org/10.1016/j.combustflame.2018.07.004
23. Zhang X, Li Y, Cao C, Zou J, Zhang Y, Li W, Li T, Yang J, Dagaut P (2019) New insights into propanal oxidation at low temperatures: an experimental and kinetic modeling study. Proc Combust Inst 37:565–573. https://doi.org/10.1016/j.proci.2018.06.173
24. Liao H, Tao T, Sun W, Hansen N, Yang B (2021) Isomer-specific speciation behaviors probed from premixed flames fueled by acetone and propanal. Proc Combust Inst 38:2441–2448. https://doi.org/10.1016/j.proci.2020.06.221
25. Gong J, Zhang S, Cheng Y, Huang Z, Tang C, Zhang J (2015) A comparative study of n -propanol, propanal, acetone, and propane combustion in laminar flames. Proc Combust Inst 35:795–801. https://doi.org/10.1016/j.proci.2014.05.066
26. Healy D, Donato NS, Aul CJ, Petersen EL, Zinner CM, Bourque G, Curran HJ (2010) n-Butane: Ignition delay measurements at high pressure and detailed chemical kinetic simulations. Combust Flame 157:1526–1539. https://doi.org/10.1016/j.combustflame.2010.01.016
27. Healy D, Kopp MM, Polley NL, Petersen EL, Bourque G, Curran HJ (2010) Methane/ *n* -Butane ignition delay measurements at high pressure and detailed chemical kinetic simulations. Energy Fuels 24:1617–1627. https://doi.org/10.1021/ef901292j
28. Healy D, Kalitan DM, Aul CJ, Petersen EL, Bourque G, Curran HJ (2010) Oxidation of C1–C5 alkane quinternary natural gas mixtures at high pressures. Energy Fuels 24:1521–1528. https://doi.org/10.1021/ef9011005
29. Kéromnès A, Metcalfe WK, Heufer KA, Donohoe N, Das AK, Sung C-J, Herzler J, Naumann C, Griebel P, Mathieu O, Krejci MC, Petersen EL, Pitz WJ, Curran HJ (2013) An experimental and detailed chemical kinetic modeling study of hydrogen and syngas mixture oxidation at elevated pressures. Combust Flame 160:995–1011. https://doi.org/10.1016/j.combustflame.2013.01.001
30. Somers KP, Simmie JM, Gillespie F, Conroy C, Black G, Metcalfe WK, Battin-Leclerc F, Dirrenberger P, Herbinet O, Glaude P-A, Dagaut P, Togbé C, Yasunaga K, Fernandes RX, Lee C, Tripathi R, Curran HJ (2013) A comprehensive experimental and detailed chemical kinetic modelling study of 2,5-dimethylfuran pyrolysis and oxidation. Combust Flame 160:2291–2318. https://doi.org/10.1016/j.combustflame.2013.06.007
31. Ranzi E, Frassoldati A, Stagni A, Pelucchi M, Cuoci A, Faravelli T (2014) Reduced kinetic schemes of complex reaction systems: fossil and biomass-derived transportation fuels: reduced kinetic schemes of complex reaction systems. Int J Chem Kinet 46:512–542. https://doi.org/10.1002/kin.20867
32. Ranzi E, Cavallotti C, Cuoci A, Frassoldati A, Pelucchi M, Faravelli T (2015) New reaction classes in the kinetic modeling of low temperature oxidation of n-alkanes. Combust Flame 162:1679–1691. https://doi.org/10.1016/j.combustflame.2014.11.030
33. Ranzi E, Frassoldati A, Grana R, Cuoci A, Faravelli T, Kelley AP, Law CK (2012) Hierarchical and comparative kinetic modeling of laminar flame speeds of hydrocarbon and oxygenated fuels. Prog Energy Combust Sci 38:468–501. https://doi.org/10.1016/j.pecs.2012.03.004
34. Chang AY, Bozzelli JW, Dean AM (2000) Kinetic analysis of complex chemical activation and unimolecular dissociation reactions using QRRK theory and the modified strong collision approximation. Z Phys Chem 214:1533
35. Chin C-H, Lee S-H (2012) Comparison of two-body and three-body decomposition of ethanedial, propanal, propenal, *n* -butane, 1-butene, and 1,3-butadiene. J Chem Phys 136:024308. https://doi.org/10.1063/1.3675682
36. Gimondi I, Cavallotti C, Vanuzzo G, Balucani N, Casavecchia P (2016) Reaction dynamics of O(^{3}P) + Propyne: II. primary products, branching ratios, and role of intersystem crossing from Ab Initio coupled triplet/singlet potential energy surfaces and statistical calculations. J Phys Chem A 120:4619–4633. https://doi.org/10.1021/acs.jpca.6b01564
37. Cavallotti C, Pelucchi M, Frassoldati A (2019) Analysis of acetic acid gas phase reactivity: rate constant estimation and kinetic simulations. Proc Combust Inst 37:539–546. https://doi.org/10.1016/j.proci.2018.06.137
38. Caracciolo A, Vanuzzo G, Balucani N, Stranges D, Casavecchia P, Pratali Maffei L, Cavallotti C (2019) Combined experimental and theoretical studies of the O(^{3}P) + 1-Butene reaction dynamics: primary products, branching fractions, and role of intersystem crossing. J Phys Chem A 123:9934–9956. https://doi.org/10.1021/acs.jpca.9b07621
39. Vanuzzo G, Caracciolo A, Minton TK, Balucani N, Casavecchia P, de Falco C, Baggioli A, Cavallotti C (2021) Crossed-beam and theoretical studies of the O(^{3}P,^{1}D) + benzene reactions: primary products, branching fractions, and role of intersystem crossing. J Phys Chem A 125:8434–8453. https://doi.org/10.1021/acs.jpca.1c06913
40. Recio P, Alessandrini S, Vanuzzo G, Pannacci G, Baggioli A, Marchione D, Caracciolo A, Murray VJ, Casavecchia P, Balucani N, Cavallotti C, Puzzarini C, Barone V (2022) Intersystem crossing in the entrance channel of the reaction of O(3P) with pyridine. Nat Chem 14:1405–1412. https://doi.org/10.1038/s41557-022-01047-3
41. Cavallotti C, Leonori F, Balucani N, Nevrly V, Bergeat A, Falcinelli S, Vannuzzo S, Casavecchia P (2014) Relevance of the channel leading to Formaldehyde + Triplet Ethylidene in the O(^{3}P) + Propene reaction under combustion conditions. J Phys Chem Lett 5:4213–4218. https://doi.org/10.1021/jz502236y
42. Leonori F, Balucani N, Nevrly V, Beargeat A, Falcinelli S, Vannuzzo S, Casavecchia P, Cavallotti C (2015) Experimental and theoretical studies on the dynamics of the O(^{3}P) + propene reaction: primary products, branching ratios, and role of intersystem

crossing. J Phys Chem C 119:14632–14652. https://doi.org/10.1021/jp512670y
43. Klippenstein SJ, Cavallotti C (2019) Ab initio kinetics for pyrolysis and combustion systems. Comput Aided Chem Eng 45:115–167
44. Chai J-D, Head-Gordon M (2008) Long-range corrected hybrid density functionals with damped atom–atom dispersion corrections. Phys Chem Chem Phys 10:6615–6620. https://doi.org/10.1039/B810189B
45. Martin JML (1996) Ab initio total atomization energies of small molecules — towards the basis set limit. Chem Phys Lett 259:669–678. https://doi.org/10.1016/0009-2614(96)00898-6
46. Cavallotti C, Della Libera A, Zhou C-W, Recio P, Caracciolo A, Balucani N, Casavecchia P (2022) Crossed-beam and theoretical studies of multichannel nonadiabatic reactions: branching fractions and role of intersystem crossing for $O(^3P)$ + 1,3-butadiene. Faraday Discuss 238:161–182. https://doi.org/10.1039/D2FD00037G
47. Ruscic B, Pinzon RE, Morton ML, von Laszevski G, Bittner SJ, Nijsure SG, Amin KA, Minkoff M, Wagner AF (2004) Introduction to active thermochemical tables: several "key" enthalpies of formation revisited. J Phys Chem A 108:9979–9997. https://doi.org/10.1021/jp047912y
48. Ruscic B, Pinzon RE, von Laszewski G, Kodeboyina D, Burcat A, Leahy D, Montoy D, Wagner AF (2005) Active thermochemical tables: thermochemistry for the 21st century. J Phys Conf Ser 16:561–570. https://doi.org/10.1088/1742-6596/16/1/078
49. Georgievskii Y, Miller JA, Burke MP, Klippenstein SJ (2013) Reformulation and solution of the master equation for multiple-well chemical reactions. J Phys Chem A 117:12146–12154. https://doi.org/10.1021/jp4060704
50. Cavallotti C, Pelucchi M, Georgievskii Y, Klippenstein SJ (2019) EStokTP: electronic structure to temperature- and pressure-dependent rate constants—a code for automatically predicting the thermal kinetics of reactions. J Chem Theory Comput 15:1122–1145. https://doi.org/10.1021/acs.jctc.8b00701
51. Klippenstein SJ (1992) Variational optimizations in the Rice–Ramsperger–Kassel–Marcus theory calculations for unimolecular dissociations with no reverse barrier. J Chem Phys 96:367–371. https://doi.org/10.1063/1.462472
52. Georgievskii Y, Klippenstein SJ (2003) Transition state theory for multichannel addition reactions: multifaceted dividing surfaces. J Phys Chem A 107:9776–9781. https://doi.org/10.1021/jp034564b
53. Klippenstein SJ, Georgievskii Y, Harding LB (2006) Predictive theory for the combination kinetics of two alkyl radicals. Phys Chem Chem Phys 8:1133. https://doi.org/10.1039/b515914h
54. Georgievskii Y, Klippenstein SJ (2003) Variable reaction coordinate transition state theory: analytic results and application to the C_2H_3+H→C_2H_4 reaction. J Chem Phys 118:5442–5455. https://doi.org/10.1063/1.1539035
55. Jasper AW (2020) "Third-body" collision parameters for hydrocarbons, alcohols, and hydroperoxides and an effective internal rotor approach for estimating them. Int J Chem Kinet 52:387–402. https://doi.org/10.1002/kin.21358
56. Frisch MJ, Trucks GW, Schlegel HB, Scuseria GE, Robb MA, Cheeseman JR, Scalmani G, Barone V, Petersson GA, Nakatsuji H, Li X, Caricato M, Marenich AV, Bloino J, Janesko BG, Gomperts R, Mennucci B, Hratchian HP, Ortiz JV, Izmaylov AF, Sonnenberg JL, Williams-Young D, Ding F, Lipparini F, Egidi F, Goings J, Peng B, Petrone A, Henderson T, Ranasinghe D, Zakrzewski VG, Gao J, Rega N, Zheng G, Liang W, Hada M, Ehara M, Toyota K, Fukuda R, Hasegawa J, Ishida M, Nakajima T, Honda Y, Kitao O, Nakai H, Vreven T, Throssell K, Montgomery JA (2016) Gaussian 09, Revision A.02. Gaussian Inc, Wallingford
57. Werner H-J, Knowles PJ, Manby FR, Black JA, Doll K, Heßelmann A, Kats D, Köhn A, Korona T, Kreplin DA, Ma Q, Miller TF, Mitrushchenkov A, Peterson KA, Polyak I, Rauhut G, Sibaev M (2020) The Molpro quantum chemistry package. J Chem Phys 152:144107. https://doi.org/10.1063/5.0005081
58. Bagheri G, Ranzi E, Pelucchi M, Parente A, Frassoldati A, Faravelli T (2020) Comprehensive kinetic study of combustion technologies for low environmental impact: MILD and OXY-fuel combustion of methane. Combust Flame 212:142–155. https://doi.org/10.1016/j.combustflame.2019.10.014
59. Cuoci A, Frassoldati A, Faravelli T, Ranzi E (2015) OpenSMOKE++: An object-oriented framework for the numerical modeling of reactive systems with detailed kinetic mechanisms. Comput Phys Commun 192:237–264. https://doi.org/10.1016/j.cpc.2015.02.014
60. da Silva G, Bozzelli JW (2006) Enthalpies of formation, bond dissociation energies, and molecular structures of the n-Aldehydes (Acetaldehyde, Propanal, Butanal, Pentanal, Hexanal, and Heptanal) and their Radicals. J Phys Chem A 110:13058–13067. https://doi.org/10.1021/jp063772b
61. Klippenstein SJ, Harding LB, Ruscic B (2017) Ab initio computations and active thermochemical tables hand in hand: heats of formation of core combustion species. J Phys Chem A 121:6580–6602. https://doi.org/10.1021/acs.jpca.7b05945
62. Active Thermochemical Tables v. 1.1124. https://atct.anl.gov/Thermochemical%20Data/version%201.124/.
63. Zhu L, Tang Y, Chen Y, Cronin T (2009) Wavelength-dependent photolysis of C3–C7 Aldehydes in the 280–330 nm region. Spectrosc Lett 42:467–478. https://doi.org/10.1080/00387010903267195
64. Baggott JE, Frey HM, Lightfoot PD, Walsh R (1987) Reactions of the formyl radical with alkyl radicals. J Phys Chem 91:3386–3393. https://doi.org/10.1021/j100296a057
65. Harding L, Klippenstein SJ, Georgievskii Y (2007) On the combination reactions of hydrogen atoms with resonance-stabilized hydrocarbon radicals. J Phys Chem A 111:3789–3801
66. Tsang W, Hampson RF (1986) Chemical kinetic data base for combustion chemistry. Part I. Methane and related compounds. J Phys Chem Ref Data 15:1087–1279. https://doi.org/10.1063/1.555759